Journal of Power Sources 196 (2011) 4242–4250

Contents lists available at ScienceDirect

Journal of Power Sources

journal homepage: www.elsevier.com/locate/jpowsour

Physico-chemical study of the degradation of membrane-electrode assemblies in a proton exchange membrane fuel cell stack

P. Ferreira-Aparicio[a,*], B. Gallardo-López[a], A.M. Chaparro[a], L. Daza[a,b]

[a] Centro de Investigaciones Energéticas, Medioambientales y Tecnológicas (CIEMAT), Avda. Complutense, 22, E-28040 Madrid, Spain
[b] Instituto de Catálisis y Petroleoquímica (CSIC), C/Marie Curie, 2, Campus de Cantoblanco, E-28049 Madrid, Spain

ARTICLE INFO

Article history:
Received 28 July 2010
Received in revised form 19 October 2010
Accepted 19 October 2010
Available online 28 October 2010

Keywords:
PEMFC stack
Membrane-electrode assembly (MEA) degradation
Postmortem analysis
Ultramicrotome-sectioned samples for TEM
XPS analysis

ABSTRACT

A proton exchange membrane fuel cell stack integrated by 8-elements has been evaluated in an accelerated stress test. The application of techniques such as TEM analyses of ultramicrotome-sliced sections of some samples and XRD, XPS and TGA of spent electrodes reveal the effects of several degradation processes contributing to reduce the cells performance. The reduction of the Pt surface area at the cathode is favored by the oxidation of carbon black agglomerates in the catalytic layer, the agglomeration of Pt particles and by the partial dissolution of Pt, which migrates towards the anode and precipitates within the membrane. In the light of the TEM, EDAX and XPS results, two combined effects are probably responsible of the increase of the internal resistance of the stack cells: (i) a lower proton conductivity of the membranes due to the high affinity of the sulfonic acid groups for ions originated from Pt crystallites and other peripherical elements such as the silicone elastomeric gaskets and (ii) the increment of electrically isolated islands in the cathode gas diffusion electrodes resulting from carbon corrosion and the degradation of the perfluorinated polymers. Water accumulation and inhomogeneous gas distribution throughout the stack cells originate different degradation rates in them.

1. Introduction

The analysis of the degradation mechanisms affecting the life and the long-term performance of proton exchange membrane fuel cells (PEMFC) is a subject of growing interest [1]. Extensive recent reviews concerning the durability of catalysts [2–6], membrane-electrode assemblies (MEAs) [7], and PEMFC performance [8,9] identify numerous stressors and degradation mechanisms. However, much more effort is needed to analyze the ageing of the several PEMFC components, establish mitigation strategies and extend their useful life. The use of accelerated stress tests has been proved to be a useful tool to assess the durability of the PEMFC components. Using this strategy, performance losses and component damages can be more efficiently analyzed under specific working conditions than applying costly and time-consuming steady-state lifetime tests [5,7].

The main degradation processes in MEAs include Pt sintering, agglomeration and redistribution, corrosion of the carbon support in the electrodes, chemical and structural degradation of the membrane, and poisonous effects aroused by contaminants from external components. As demonstrated by many researchers, agglomeration and particle growth of nanostructured Pt is the most dominant mechanism for catalyst degradation in PEM fuel cells. Virkar and Zhou [10] have explained that Ostwald ripening, involving coupled transport of electrically charged species, is the main reason for particle growth in Pt/C catalysts, where the Pt is transported through the liquid and/or through the ionomer and the electrons through the carbon support. Other groups [11,12] believe that two other mechanisms are predominately responsible for degradation: Pt particles detaching from the support and dissolving into the electrolyte without re-deposition, and/or a combination of Pt particle coalescence and Pt solution/re-precipitation within the solid ionomer. Whatever mechanism the particle growth follows, dissolution of Pt is an important step during the catalyst degradation process.

Many groups have reported the presence of Pt particles inside the PEM as well as enrichment of Pt in the catalytic layer-membrane interface under different conditions [13–19]. These Pt particles originate from the dissolved Pt species, which diffuse in the ionomer phase and subsequently precipitate in the ionomer phase of the electrode or in the membrane. The precipitation probably occurs via the reduction of Pt ions by hydrogen that has crossed over from the anode. Concerning the direction and degree of the Pt particle migration and redistribution, the results presented in current literature are not always consistent. Bi and Fuller [20], Fer-

* Corresponding author. Tel.: +34 91 3460897; fax: +34 91 3466269.
E-mail address: paloma.ferreira@ciemat.es (P. Ferreira-Aparicio).

0378-7753/$ – see front matter © 2010 Elsevier B.V. All rights reserved.
doi:10.1016/j.jpowsour.2010.10.059

reira et al. [19] and More et al. [12] observed Pt enrichment at the cathode/membrane interface or near the cathode, while Xie et al. [21] and Guilminot et al. [22] observed Pt enrichment at the anode/membrane interface. The main reason for the diversity of results could be that Pt migration and redistribution is a complex process affected by many factors such as potential, operating time, potential cycle numbers, cell operating conditions, gas permeability of the membrane, and so on. Therefore, more detailed explanations of the Pt redistribution and its effect on the cell performance are needed for a more profound understanding of the specific characteristics of Pt catalysts behavior during operation. It should be also considered that the presence of Pt is known to accelerate the degradation processes of carbon and polymers in its vicinity [23–25].

Most of the degradation studies in the literature are performed on single cells where thermal and fluids management is simpler and the operation conditions are more easily controllable than in PEMFC stacks. The arrangement in a stack usually difficults the operation due to uneven flow distribution. When a common feed stream is used to supply gas to all cells, it is difficult to guarantee that all cells will receive the same gas flow rate. Furthermore, a non-uniform temperature within the cells of the stack during operation aggravates the gas distribution inhomogeneity. Once a cell has water built-up, less gas will flow to that cell. This situation may originate reactant-starved conditions that in a stack can lead to cell potential reversal and irreversible damages [26].

MEA contamination from trace metals can occur throughout the fuel cell too and excess water in the system can greatly increase contamination, allowing transport or leaching metals out of the stack or system. The membrane is an especially vulnerable component due to the sulfonic acid group's affinity for foreign cations, which can exchange protons, modify its bulk properties such us ionic conductivity, transference numbers or water content, and originate the cell voltage drop [27]. Just a few studies analyze the degradation behavior of different MEAs in a PEMFC stack by characterizing them after dismantling the unit [28–30]. This study attempts to analyze the evolution of the degradation of the MEAs components in an 8-elements stack. An accelerated stress test (AST) has been used to force faster degradation of cells. *Post-mortem* analyses of some of the MEAs in the stack have been performed using techniques such as X-ray diffraction (XRD), transmission electron microscopy (TEM), X-ray photoelectron spectroscopy (XPS) or thermogravimetric analysis (TGA), which reveal some of the consequences of the degradation under operation conditions. In the light of these results some strategies are proposed to improve durability of the damaged components.

2. Experimental

An 8-elements stack has been set up for the study. Symmetrical membrane-electrode assemblies were prepared using commercial electrodes from BASF (ELAT GDE LT250EWALTSI) with a Pt loading of 0.25 mg cm^{-2}. The electrolyte was Nafion NRE212 membrane in its acid form. Before the assembly, pre-cut membrane pieces were activated and expanded in ultrapure deionized water. Two stainless steel end plates with 8 bolts distributed around their external perimeter were used as clamping elements. Terminal and bipolar flow field plates were made up of graphite (2 mm thick) with double parallel serpentine flow-field paths.

The assembly of the stack was performed in a clean compartment with a highly humid atmosphere that is controlled to prevent membrane drying and shrinking. Once fixed the exhaust end-plate to a workbench, two tie rods were inserted in it for aligning the following stacked elements. Insulating gaskets of silicon elastomer were used as sealings for the module. Once aligned the successive cells consisting in a MEA between two flow field plates, the upper gold-plated current collector and the inlet end-plate were assembled. The stack was then tightened by screws at a torque of 3 N m. Crossover and leak flows were checked to be negligible before testing the stack.

The module was operated with H_2 and O_2 at fixed stoichiometries under continuous flow. No heating elements were used. The overall temperature of the stack was determined by using two thermocouples oppositely located at both end-plates. The measured temperature was automatically controlled below 323 K by a fan fixed below the support structure. The maximum overall temperature of 323 K was reached at current densities above 0.2 A cm^{-2}. Local differences of temperature, which were expected in the stack within each cell and among the cells (mainly between those located at the center of the stack and those closer to the end-plates), could not be determined with the available setup. Both streams were humidified at room temperature in glass saturators.

An AST consisting in three consecutive operational/standby periods of 8 h/16 h was applied for the study. During the operational periods, the stack was submitted to different feeding stoichiometries ($\lambda_{H_2}/\lambda_{O_2}$: 1.5/3.0; 3.5/8.0; 1.3/9.0). The performance under those conditions was evaluated by recording polarization curves. Then, it was operated in stationary state at constant flow, 0.8 atm backpressure and high potential with a load demand of 0.07 A cm^{-2}. The overall temperature of the stack determined at that constant demand was 315 K. Three main accelerated stressors have been applied during the AST: (i) a high operational potential under stationary conditions (constant load of 0.07 A cm^{-2}, which generates an overall temperature in the stack of 42 °C), (ii) humidification of the feed streams at room temperature below the stack operational temperature, and (iii) the use of too high O_2 stoichiometry ($\lambda_{O_2} \gg 3.5$) or too low H_2 stoichiometry ($\lambda_{H_2} < 1.5$).

As a reference for performance comparison, a single cell test was performed with a MEA integrated by the same components and operated at $\lambda_{H_2}/\lambda_{O_2}$: 1.5/3.0 and 1 atm backpressure. In this case, the fed streams were humidified at the operation temperature, which was maintained constant a 353 K by using heating elements integrated in the end-plates.

After evaluation, the stack was disassembled to analyze the degradation of the used components. Characterization of the used electrodes was performed by X-ray diffraction (XRD), transmission electron microscopy (TEM), X-ray photoelectron spectroscopy (XPS) and thermogravimetric analysis (TGA). After disassembling the stack, MEAs were carefully recovered and electrodes were separated from the NRE212 membrane to be analyzed. A volume average diameter was estimated from the broadening of the Pt XRD line corresponding to the (2 2 0) plane ($2\theta = 65.7°$). Diffractograms were recorded in a Seifert XRD 3000P instrument in the 2–80° 2θ range in a continuous scan mode with Cu Kα radiation ($\lambda = 1.540\,598$ Å).

Cross-sectional specimens for TEM observation were prepared by ultramicrotomy. A small piece of the MEA was embedded in Spur epoxy resin and dried for 48 h at 343 K. The sample was then sliced by an ultramicrotome (Reichert Ultracut E) using a diamond knife (Diatome) at room temperature. The thickness of the sample was about 30–60 nm. The sliced specimen was supported on a conventional ⌀3 mm Cu mesh with a carbon micro-grid. TEM observations were performed using a Jeol JEM-2100F transmission electron microscope equipped with an energy dispersive X-ray spectroscopy (EDS) system. The TEM was operated at an accelerating voltage of 200 kV.

XPS analyses were performed in a Perkin-Elmer PHI 5400 spectrometer. The excitation source was the Mg Kα line ($h\nu = 1253.6$ eV) with a spot size of 1 mm^2. The pressure in the analysis chamber was kept below 10^{-9} Torr during acquisition.

Finally, some of the used electrodes and membranes were characterized by thermal analysis. Mass losses in the samples

were determined with a Mettler thermobalance (Toledo STAR SW 9.01), whereas the effluent gas was analyzed with a quadrupole mass spectrometer (Pfeiffer Vacuum Omnistar) equipped with channeltron and faraday detectors. The ion currents for several mass-to-charge ratios in the range between 2 and 100 were registered with time. Gas diffusion electrodes were analyzed by temperature programmed oxidation under a continuous O_2/N_2 flow of 1.2 l h^{-1}.

3. Results and discussion

3.1. Stack operation during AST

The stack has been operated using a different feeding stoichiometry ($\lambda_{H_2}/\lambda_{O_2}$) during the each of the three operational periods. The stoichiometry change induces considerable differences in the water management process among the cells. Fig. 1 includes the individual polarization curves under each feeding condition together with an *I–V* curve obtained for a single cell of analogue configuration and the average polarization curve of the stack.

It can be seen that all the cells in the stack (C_1–C_8) under a typical 1.5/3.0 $\lambda_{H_2}/\lambda_{O_2}$ stoichiometry reduce their performance in comparison with an identical MEA in a single cell test (C_{Ref}) (Fig. 1a). At a fixed current density of 0.5 A cm^{-2}, the voltage of the different cells of the stack lays within the range 0.35–0.68 V, being 0.67 V the voltage of the C_{Ref} under those conditions. At low current densities, only C_6 shows poorer performance, whereas at current densities above 0.25 A cm^{-2} the cells C_4 and C_8 deviate from the general trend too.

By increasing the $\lambda_{H_2}/\lambda_{O_2}$ stoichiometries up to 3.5/8.0 several cells improve their behavior. Most individual polarization curves are fairly close to that obtained for C_{Ref}. The three cells showing lower performance in this case (C_5, C_7, C_8) are not the same than in the previous case with lower λ_{H_2} and λ_{O_2} stoichiometries. In particular, the last cell of the stack is the one showing poorer performance. The origin of this decay is at this point merely speculative with the known variables; membrane damage, contamination, electrodes flooding, or a combination of several effects could be among the causes of this performance loss.

By changing $\lambda_{H_2}/\lambda_{O_2}$ to 1.3/9.0 (Fig. 1c) fluids management in the stack is aggravated as compared with previous cases. At current densities above 0.45 A cm^{-2}, *I–V* curves show a slope change for most cells due to a concentration polarization attributable to the low H_2 stoichiometry. At low current densities, the two last cells (C_7 and C_8) reduce their open circuit voltage (OCV) as shown in their polarization curves.

Fig. 2 summarizes the voltage for each cell in the stack at 0.5 A cm^{-2} under the different feeding conditions in comparison with that obtained for the reference cell. By analyzing the voltage in the cells of the stack, the performance improvement using higher $\lambda_{H_2}/\lambda_{O_2}$ stoichiometries is evidenced. The use of reduced H_2 excess originates lower performance for the cells in the extremes of the stack.

Fig. 2 summarizes the voltage for each cell in the stack at 0.5 A cm^{-2} under the different feeding conditions in comparison with that obtained for the reference cell. By analyzing the voltage in the cells of the stack, the performance improvement using higher $\lambda_{H_2}/\lambda_{O_2}$ stoichiometries is evidenced. The use of reduced H_2 excess originates lower performance for the cells in the extremes of the stack, where anode flooding is probably favored by a lower temperature than in those located in central positions.

Using $\lambda_{H_2}/\lambda_{O_2}$ stoichiometry of 1.3/9.0 for the stationary stack operation, some cells (C_3 and C_4) experiment a voltage reversal at low constant load demand (0.1 A cm^{-2}) not observed under other

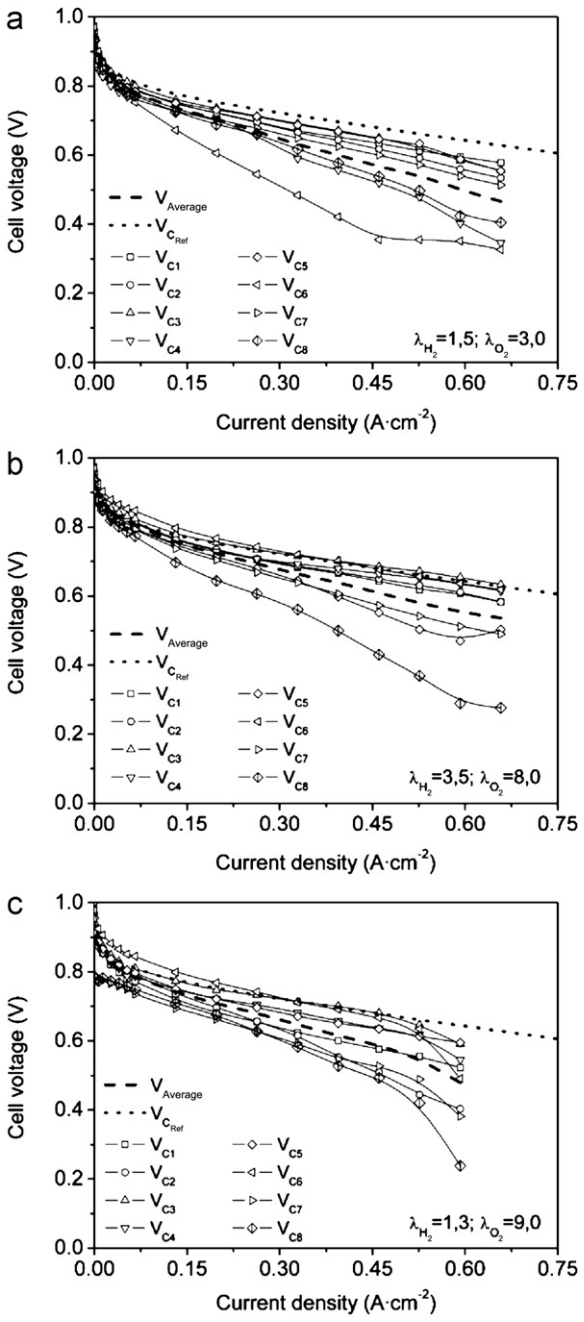

Fig. 1. Individual polarization curves obtained for the 8-element stack at 0.8 atm backpressure and different feeding stoichiometric conditions: (a) $\lambda_{H_2}/\lambda_{O_2}$: 1.5/3.0, first operational period, 20 h after initial start-up; (b) $\lambda_{H_2}/\lambda_{O_2}$: 3.5/8.0, second operational period, 40 h after initial start-up; (c) $\lambda_{H_2}/\lambda_{O_2}$: 1.3/9.0, third operational period, 60 h after initial start-up. The average polarization curve obtained for the stack and a reference obtained in a single cell test for an analogue MEA are also represented for comparison.

feeding conditions. This condition of reduced H_2 excess ($\lambda_{H_2} = 1.3$) originates a fast performance loss and irreversible damages in the stack. Among the stressors applied in the AST, the reduced λ_{H_2} can be considered to be the one originating a faster degradation. Below a certain limit, the unconverted H_2 in the anodic stream may be not enough to remove water effectively from some anodic regions and flooded zones are susceptible of being directly oxidized due to fuel starvation.

In order to evaluate the performance loss after the AST, a last polarization curve was measured applying the conditions of the first operational period ($\lambda_{H_2}/\lambda_{O_2}$: 1.5/3.0, room temperature

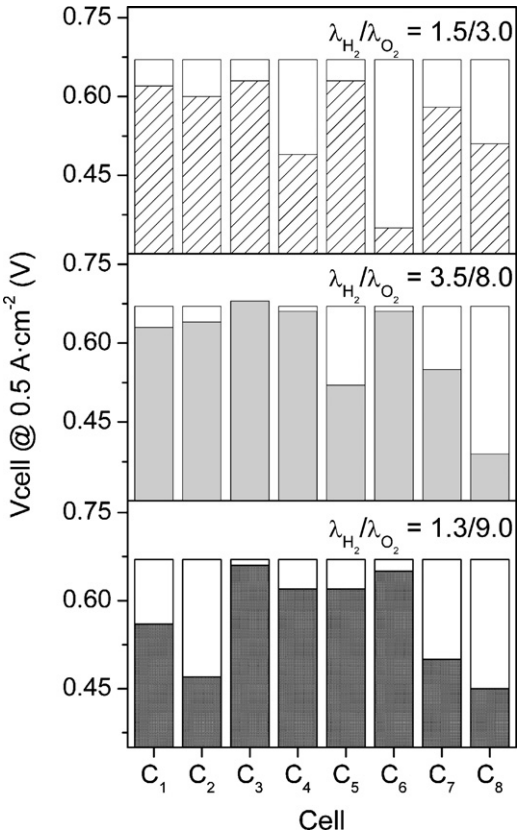

Fig. 2. Voltage of each cell of the stack at 0.5 A cm^{-2} in comparison with that of a single cell under different $\lambda_{H_2}/\lambda_{O_2}$ feeding conditions.

humidification, and overall temperature in the stack of 323 K). By comparing the first and last polarization and power curves, which are presented together in Fig. 3, the irreversible degradation underwent by the stack can be clearly appreciated. Ohmic losses are substantially increased and the stack performance is drastically reduced.

A visual examination of the cells of the stack after being disassembled only revealed apparent damages in cells C_3 and C_4, whose anodes where cracked, thinner and partially adhered to the bipolar plate. The damage in those cells contrasts with their good performance under operation using high $\lambda_{H_2}/\lambda_{O_2}$ stoichiometry. No evident alterations were observed in other MEAs.

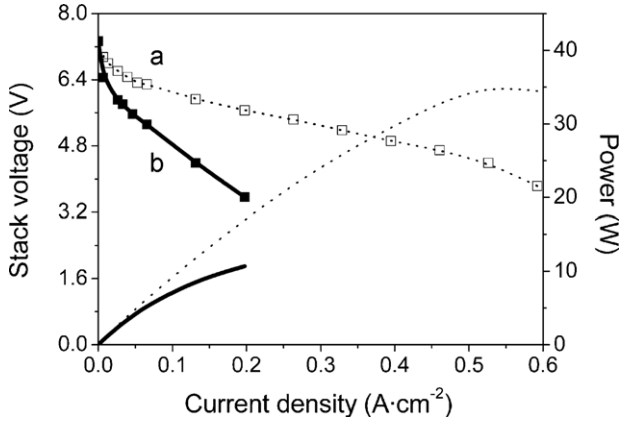

Fig. 3. Polarization and power curves obtained at 0.8 atm backpressure for the stack before (a, dotted line) and after (b, solid line) the AST. Operation conditions: $\lambda_{H_2}/\lambda_{O_2}$: 1.5/3.0; T_{stack}: 323 K.

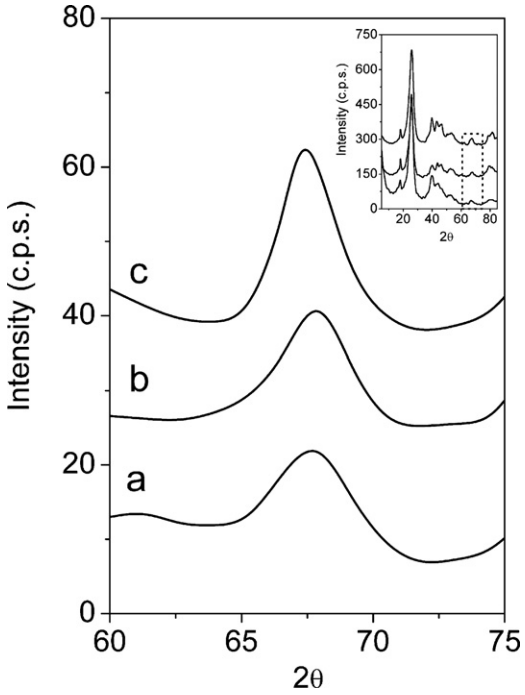

Fig. 4. X-ray diffractograms obtained for the [2 0 0] plane of Pt crystallites at $2\theta = 67.5^\circ$ in: (a) pristine GDE; (b) aged C_4 anode; (c) aged C_4 cathode.

3.2. Physico-chemical characterization

Different techniques have been applied for the detailed investigation of the damages suffered by the MEAs in the stack. The changes in the catalytic layers have been firstly analyzed by XRD in order to determine the average Pt particle size of the used electrodes. The bulk average particle size has been estimated for pristine and degraded electrodes by analyzing the broadening of the X-ray diffraction line corresponding to the [2 0 0] plane of Pt crystallites at $2\theta = 67.5^\circ$. Fig. 4 presents the [2 0 0] Pt diffraction line for the anode and cathode in C_4 in comparison with that obtained for a pristine GDE. Little change in the Pt diffraction line has been detected in the anode, whose mean particle size has been estimated to be 3.4 ± 0.2 nm, very similar to the 3.5 ± 0.2 nm obtained for the pristine electrode. A more intense diffraction peak corresponding to an estimated average value of 6.8 ± 0.4 nm has been obtained at the cathode, indicating the agglomeration of particles at the oxygen electrode.

The analysis of ultramicrotome sliced specimens of the MEAs by TEM corroborates the XRD results. As shown in Fig. 5, the analysis of the catalyst after the AST reveals that the well dispersed Pt particles of the original electrode seem to form irregular and branched beaded agglomerates in the cathode catalytic layer of the MEA. The aggregates of the carbon black support, which are well defined in the original catalyst, are much more reduced and diffused in the cathode catalytic layer. In the absence of a catalytic support, Pt nanoparticles have tendency to interact with others in order to minimize their high specific surface energy. On the base of the statistical analysis of more than one thousand particles measured in several TEM micrographs, particle size distributions have been estimated (Fig. 6). In the fresh electrodes the mean particle size defined as the median (D_{50}) of the distribution is close to 3.5 nm. The resulting differential distribution profile in the C_4 cathode indicates that a large amount of discrete particles become bunched forming larger aggregates, although many of them still maintain their original size. The mean particle size increases up to 6.9 nm in the cathode. This value perfectly agrees with XRD measurements.

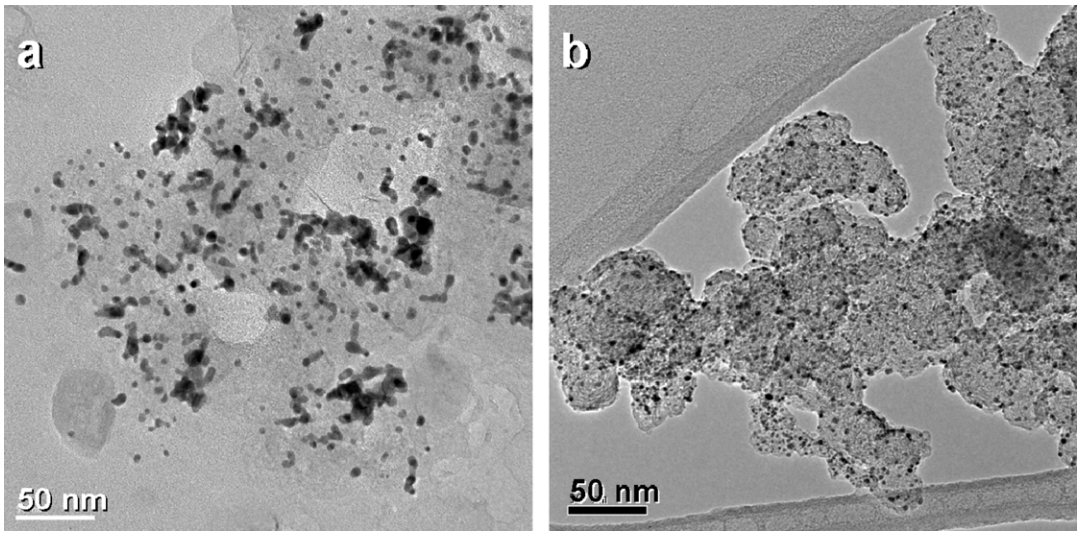

Fig. 5. TEM micrographs obtained from the catalyst in (a) the aged C_4 cathode and (b) a pristine electrode.

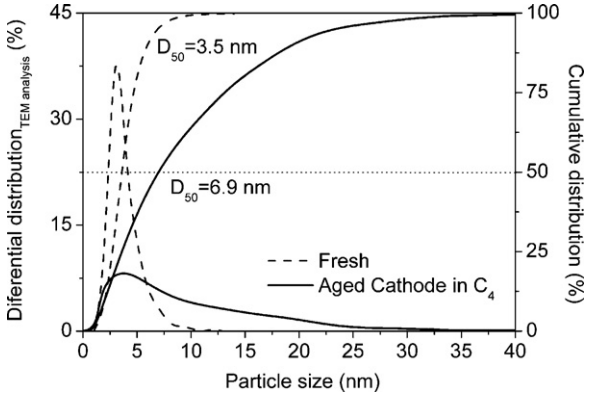

Fig. 6. Differential and cumulative particle size distributions obtained from the analysis of several TEM micrographs for the catalyst in a pristine electrode (dashed line) and in the aged C_4 cathode (solid line).

As shown in Fig. 7, most of the discrete crystallites and the particles assembled in aggregates present a hexagonal 2D shape projection. Platinum catalyst nanoparticles preferentially crystallize with a face centred cubic structure (fcc) resulting in cubo-octahedral geometry with eight (1 1 1) and six (1 0 0) faces (Fig. 6c).

An examination of the zone close to the membrane-cathode interface reveals the presence of precipitated Pt particles inside the polymeric membrane (Fig. 8) and the appearance of crystalline structures with sizes in the range 30–60 nm (Fig. 9). The effects of Pt dissolution from cathode and its movement either through diffusion (cations) or due to the electric field (anions) towards the anodic side of the membrane have been analyzed by different research groups [13–24]. The location of Pt deposited inside the polymer electrolyte seems to depend on the applied potential and the H_2 and O_2 partial pressures at both sides of the membrane [31,32]. The operation under several feeding conditions and

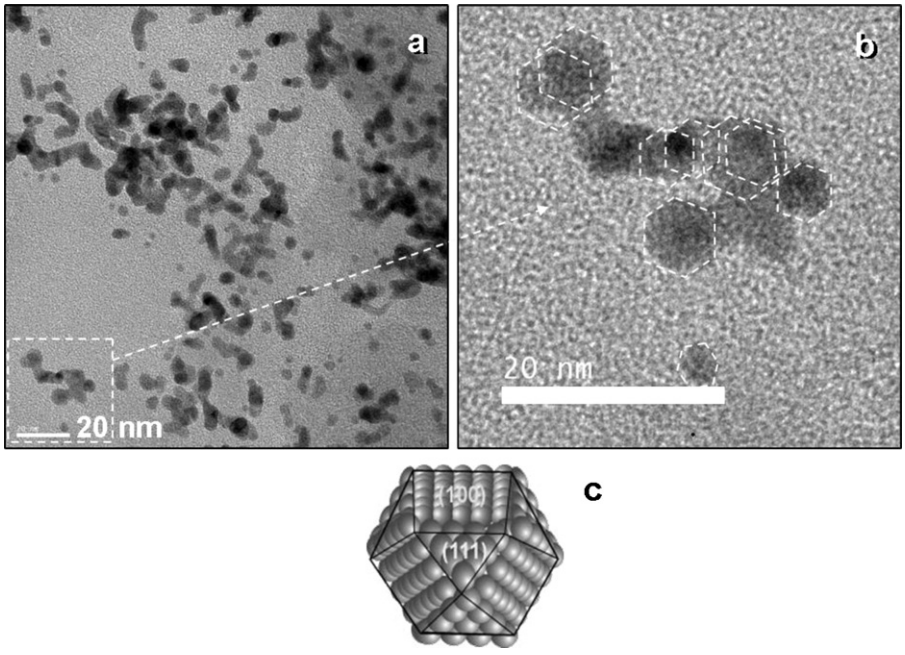

Fig. 7. (a) TEM image of the Pt/Vulcan XC72 catalyst in the aged C_4 cathode; (b) detail of an aggregate of discrete Pt particles with hexagonal 2D shape projection; (c) cubooctahedral geometry of a Pt face cubic centered (fcc) crystallite with hexagonal 2D shape projection.

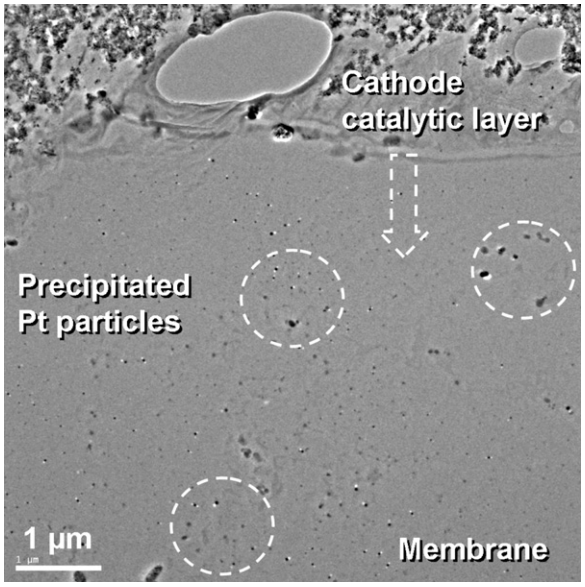

Fig. 8. TEM image obtained from an ultramicrotome sliced sample of the aged C_4 membrane-electrode assembly. Precipitated Pt particles can be appreciated in the NRE212 membrane at different distances from the cathode.

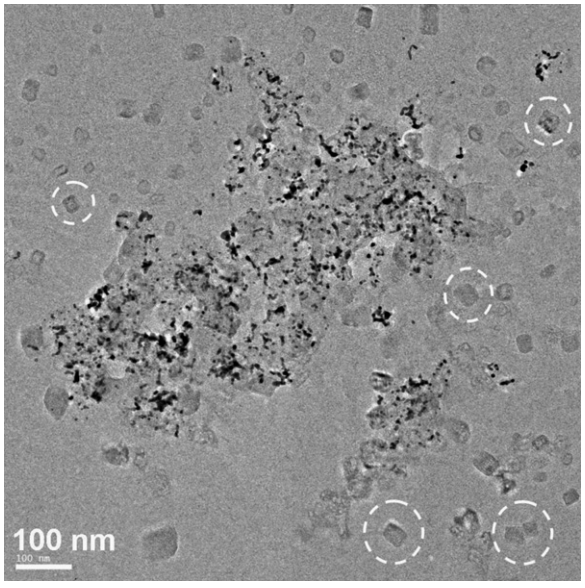

Fig. 9. TEM image from the cathode-membrane interface region of the aged C_4 MEA. Numerous crystals containing Na, K, Cl and Si can be appreciated around the catalyst.

a wide range of potentials originates a dispersion of Pt particles at different distances from the cathode, whereas operation under stationary conditions usually results in a defined band at a given distance between both electrodes. Ettingshausen et al. have suggested that platinum crystallites precipitated in the ion channels of the membrane probably decrease the proton conductivity of the membrane, increase the ohmic resistance of the cell and decrease its performance [28].

In addition to precipitated Pt, the membrane houses other crystalline structures whose composition has been analyzed by EDAX. Table 1 summarizes the compositional analysis of several zones in Fig. 9. The obtained spectra indicate the presence of Na, K, Cl and Si elements in remarkable quantities, in addition to C, F, O and S typical from the Nafion membrane. The affinity of the sulfonic acid group in the membrane and ionomer for foreign cations makes those components especially vulnerable to contamination. The exchange of proton by trace metals can modify the internal resistance of the cell and originate a voltage drop. The appearance of Si compounds in the membrane is most probably due to contamination originated from the elastomeric gaskets degradation. Si contamination has been also detected in the surface of some electrodes by X-ray photoelectron spectroscopy.

XPS analyses have been carried out for pristine electrodes and for the anodes and cathodes of some cells. Figs. 10–12 show the XPS spectra obtained in the Si 2p, F 1s and C 1s regions for the electrodes of the cells C_3 and C_7 as representative samples of cells showing different performance. It can be observed that some silicon-containing compounds are also accumulated on the electrodes surface. In particular, noticeable signals corresponding to two different states can be found mainly at the cathodes. The band at 103.7 eV is characteristic of compounds such as SiO_2 [33], whereas the signal at higher binding energy (107 eV) could be attributed to haloalkylsilanes [34–36]. In a study regarding the chemical degradation of elastomeric gasket materials in a simulated PEMFC environment, Tan et al. have shown that de-crosslinking and chain scission in the backbone is the main degradation mechanism for silicon elastomers [37]. As a matter of fact, Schulze et al. have found silicon-containing deposits in the cathode backside and on its surface [38].

By analyzing the F 1s region of the XPS spectra (Fig. 10), the degradation of the electrodes in the catalytic layers can be appreciated. Considering the signal of the pristine GDE as a reference, the fluorocarbon chain does no suffer significant alteration in the anodes. The main peak at 689 eV is attributable to the C–F binding energy in $(-CF_2-CF_2-)_n$ segments as in the polytetrafluoroethylene. A second signal at 5 eV higher binding energy (693 eV) cannot be explained by different chemical states. It can be ascribed to the splitting of the F 1s signal due to the electrical charging of the PTFE chains in the electrode by photoelectron emission [39]. Some regions containing tetrafluoroethylene chains have become probably electrically insulated from the conductive carbon black and are therefore strongly charged and shifted to higher binding energies. This effect is especially remarkable in the C_7 cathode.

By analyzing the C 1s carbon region, the same shift of 5 eV can be observed for the signal at 291.6 eV, corresponding to the C–F bonds of $(-CF_2-CF_2-)_n$ segments. The change with regard to the pristine GDE is particularly evident in the C_7 cathode, for which the splitted peak at 296 eV is especially intense. The signal at 284.5 eV, which corresponds to carbon black and is not affected by the charging

Table 1
Compositional analyses obtained by EDAX in seven different zones of the micrograph in Fig. 8.

Zone	C	O	F	Na	Si	S	Cl	K	Ca	Cu[a]	Pt
1	95.2	2.1		0.3	0.9		0.2	0.2		1.1	
2	59.4		31.9	2,8			0.9	3.0		2.0	
3	66.8		19.7	2.1	1.2	0.9	0.8	2.3	0.6	2.7	2.9
4	91.3	2.9	2.5	0.4	0.5	0.3	0.6	0.4		1.1	
5	87.9			1.7	1.3		0.9	6.7		1.5	
6	74.8	7.4		4.4	1.2		2.8	9.4			
7	94.8			1.7	0.7			1.5		1.3	

[a] Corresponding to the copper grid of the TEM sample.

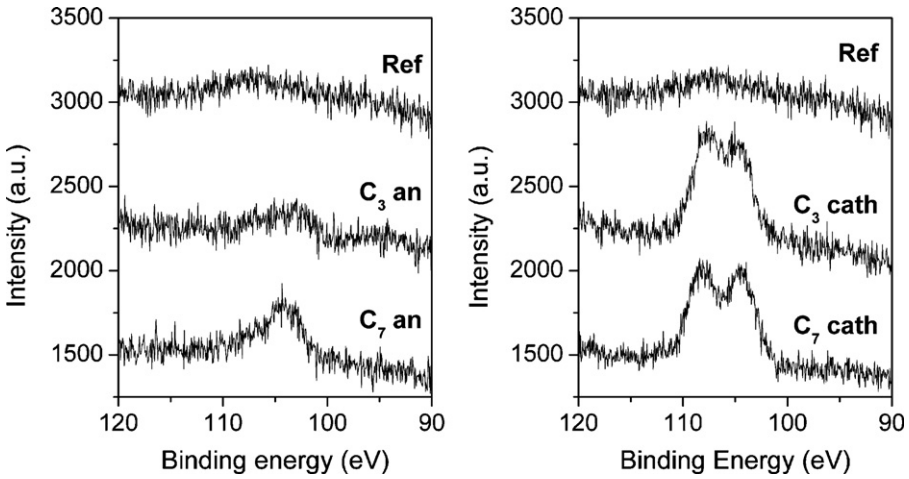

Fig. 10. XPS spectra obtained in the Si 2p region for the anodes and cathodes of the aged C_3 and C_7 MEAs in comparison with a pristine gas diffusion electrode as a reference.

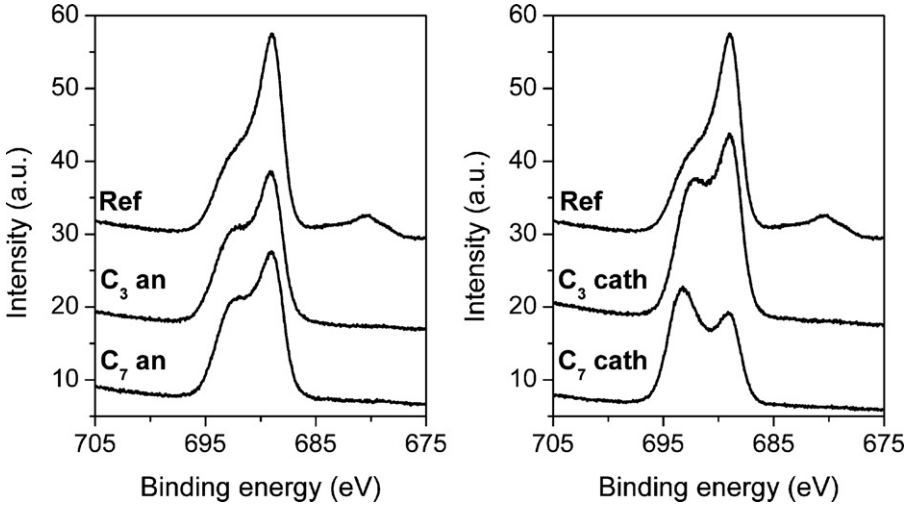

Fig. 11. XPS spectra obtained in the F 1s region for the anodes and cathodes of the aged C_3 and C_7 MEAs in comparison with a pristine gas diffusion electrode as a reference.

effect, is precisely observed to decrease in the electrode with more regions electrically insulated.

Cathode surfaces suffer remarkable modification due to the formation of less electrically conductive regions corresponding to the sulfonated polymer, but apparently no structural modification takes place. On the contrary, some anodes (in C_3 and C_4) show serious degradation of their backing, although no chemical modification is detected on its catalytic surface layer. They become thinner and stiffer, and are cracked and partially adhered to the bipolar plate in some regions.

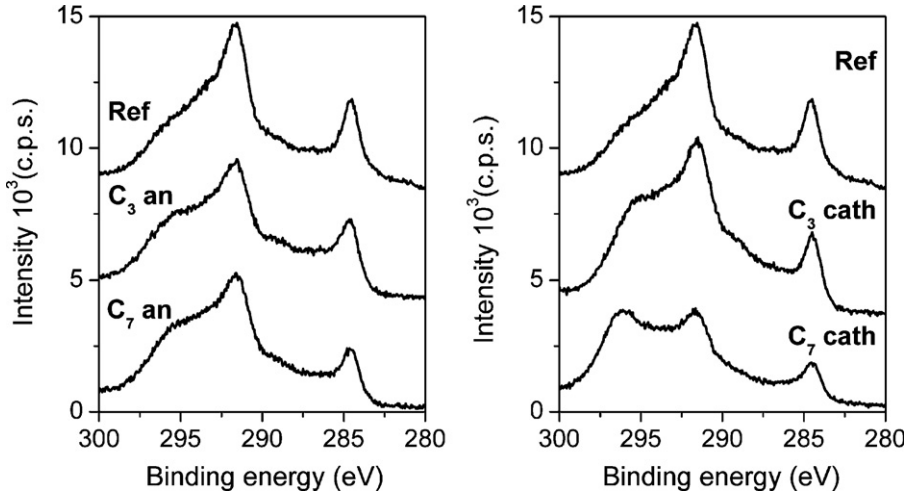

Fig. 12. XPS spectra obtained in the C 1s region for the anodes and cathodes of the aged C_3 and C_7 MEAs in comparison with a pristine gas diffusion electrode as a reference.

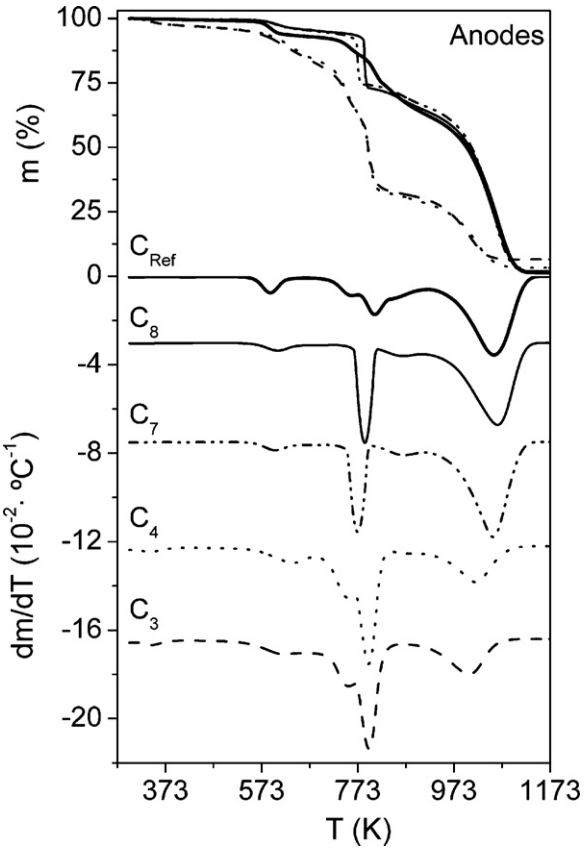

Fig. 13. Thermogravimetric analysis and differential thermogravimetry of the temperature programmed oxidation of the anodes of four representative cells of the stack (C_3, C_4, C_7, C_8) in comparison with a pristine GDE as reference.

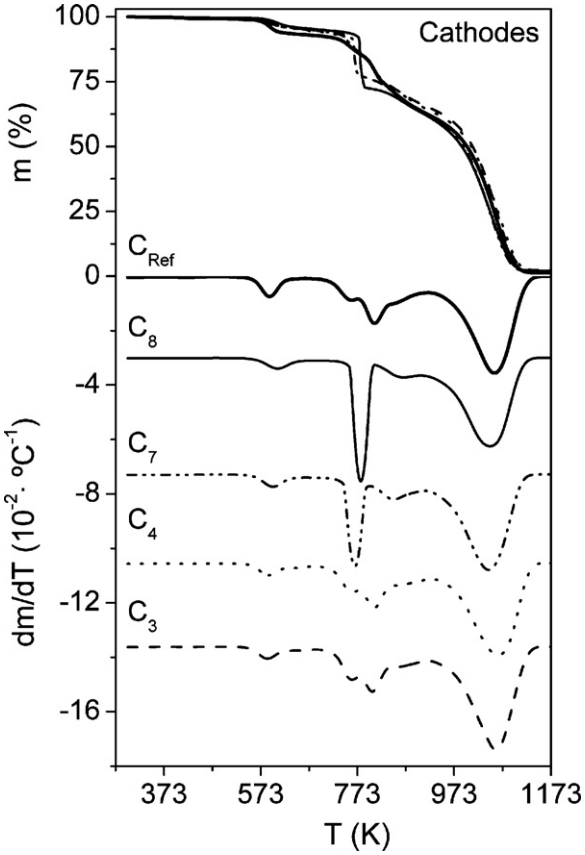

Fig. 14. Thermogravimetric analysis and differential thermogravimetry of the temperature programmed oxidation of the cathodes of four representative cells of the stack (C_3, C_4, C_7, C_8) in comparison with a pristine GDE as reference.

As a matter of fact, the thermal analysis of evidently degraded anodic GDEs reflects this situation. Fig. 13 presents the thermogravimetric curves and the differential thermogravimetric analyses under oxidizing atmosphere of several anodes from cells C_3, C_4, C_7 and C_8 in comparison with that obtained for a pristine GDE. The main oxidation processes can be observed around 600 K, 800 K and 1050 K. Based on the mass spectrometer signals, the first mass loss is due to the carbon catalyst support, whose oxidation is catalyzed by the Pt particles in its surroundings; the second one corresponds to the decomposition of the perfluorinated polymers, and finally, the mass loss above 973 K is ascribed to the carbon black and carbon fibres from the GDE backing. The marked decrease of the last mass loss in the C_3 and C_4 anodes reveals that part of that carbon in the gas diffusion layer has been oxidized and lost during the stack operation under the low H_2 stoichiometry that originated the cell potential reversal episodes. In C_3 and C_4 anodes, there is a relative increase of the mass percentage corresponding to the final residue of Pt and the amount of fluorocarbon polymers in the electrode. The shift and narrowing of the polymer decomposition process to lower temperature in the C_7 and C_8 anodes gives indication of the degradation of their perfluorinated chains. Similar polymer degradation takes place in the cathodic electrodes of the same cells (C_7 and C_8) in Fig. 14. However, no noticeable alteration is found for C_3 and C_4 cathodes.

The presented results reveal different degradation degrees in the cells integrating a stack. The origin of these differences can be attributed to the uneven distribution of the fed gases and water within the stack cells. In particular, anode flooding causes irreversible damages in anodes by fuel starvation and leads to the corrosion of the anode backings. The use of carbon fibres with higher corrosion resistance might contribute to reduce their degradation rate. The cathodic catalyst also experiments remarkable oxidation, which favor the agglomeration of the discrete Pt particles and the dissolution and migration of Pt towards the membrane. Using graphitic materials as cathodic catalytic supports could reduce the impact of these processes [25,40,41]. The presence of water in the electrodes also favors contaminant migration from peripherical components to the electrodes and the membrane. The presence of these contaminants probably contributes to increase the internal resistance of cells and decrease their performance. The use of gaskets made up of membrane compatible materials, such as Kapton, could also contribute to reduce the MEAs degradation by contaminants.

4. Conclusions

An 8-elements PEM fuel cell stack has been assembled and evaluated by applying an accelerated stress test. The complexity of the fluids management originates a large performance drop of some of the MEAs in the stack as compared to an equivalent MEA tested in a single cell. By increasing the oxygen stoichiometry a better performance has been observed, but operation at high cell voltages, low load demand and hydrogen stoichiometries below 1.5 causes accelerated and irreversible degradation of the cells in different extension. Adjusting operation parameters to improve water management in the stack is fundamental to alleviate fast degradation of the cells.

MEAs degradation has been observed to involve the cathodic catalytic layer, the membrane and the integrity of gas diffusion backings in flooded regions of some anodes. The agglomeration of individual Pt particles at the cathodic catalytic layer and the Pt migration towards the proton exchange membrane contribute

to reduce the Pt surface area in the cathodes. Furthermore, the oxidation of the carbon black support in the cathode catalytic layer reduces the electrode conductivity and favors the formation of electrically isolated islands. The polymeric membrane houses precipitated Pt crystallites migrated from the cathode and other crystals containing Si, Mg and Ca, probably originated from the silicon gaskets degradation.

The performance decay of some cells could be attributed to a combination of the following causes: (a) reduction of the cathode surface area, (b) the increase of the cell internal resistance originated by the oxidation of carbon in the cathodes and the accumulation of Pt crystallites and other ionic species in the membrane contributing to reduce to the proton conductivity, and (c) hydrophobicity loss contributing to electrode flooding. Other degradation processes such as membrane thinning or gas crossover could be also among the reasons for performance decay although no experimental evidence of their occurrence has been found. In order to mitigate the observed material degradation processes it is proposed to use graphitized carbon materials with higher corrosion resistance for cathodic catalysts and anode backings, and gaskets made up of membrane compatible materials (such as Kapton).

Acknowledgements

The authors acknowledge the Comunidad de Madrid for financial support under Programs ENERCAM (Ref. S0505/ENE-0304) and DIVERCEL (Ref. 2009/ENE-1475).

References

[1] F.A. de Bruijn, V.A.T. Dam, G.J.M. Janssen, Fuel Cells 1 (2008) 3–22.
[2] Y. Shao, G. Yin, Y. Gao, J. Power Sources 171 (2007) 558–566.
[3] X. Yu, S. Ye, J. Power Sources 172 (2007) 133–144.
[4] N. Yousfi-Steiner, Ph. Moçotéguy, D. Candussoc, D. Hissel, J. Power Sources 194 (2009) 130–145.
[5] S. Zhang, X.-Z. Yuan, J.N.C. Hin, H. Wang, K.A. Friedrich, M. Schulze, J. Power Sources 194 (2009) 588–600.
[6] X. Yu, S. Ye, J. Power Sources 172 (2007) 145–154.
[7] S. Zhang, X. Yuan, H. Wang, W. Mérida, H. Zhu, J. Shen, S. Wu, J. Zhang, Int. J. Hydrogen Energy 34 (2009) 388–404.
[8] J. Wu, X.Z. Yuan, J.J. Martin, H. Wang, J. Zhang, J. Shen, S. Wu, Walter, Mérida, J. Power Sources 184 (2008) 104–119.
[9] W. Schmittinger, A. Vahidi, J. Power Sources 180 (2008) 1–14.
[10] A.V. Virkar, Y. Zhou, J. Electrochem. Soc. 154 (2007) B540–B547.
[11] K.J.J. Mayrhofer, J.C. Meier, S.J. Ashton, G.K.H. Wiberg, F. Kraus, M. Hanzlik, M. Arenz, Electrochem. Commun. 10 (2008) 1144–1147.
[12] K.L. More, R. Borup, K.S. Reeves, ECS Trans. 3 (2006) 717–733.
[13] J. Zhang, B.A. Litteer, W. Gu, H. Liu, H.A. Gasteiger, J. Electrochem. Soc. 154 (10) (2007) B1006–B1011.
[14] J. Péron, Y. Nedellec, D.J. Jones, J. Rozière, J. Power Sources 185 (2008) 1209–1217.
[15] A. Ohma, S. Yamamoto, K. Shinohara, J. Power Sources 182 (1) (2008) 39–47.
[16] K. Yasuda, A. Taniguchi, T. Akita, T. Ioroi, Z. Siroma, Phys. Chem. Chem. Phys. 8 (2006) 746–752.
[17] T. Yoda, H. Uchida, M. Watanabe, Electrochim. Acta 52 (2007) 5997–6005.
[18] E. Guilminot, A. Corcella, M. Chatenet, F. Maillard, F. Charlot, G. Berthomé, C. Iojoiu, J.-Y. Sanchez, E. Rossinot, E. Claude, J. Electrochem. Soc. 154 (11) (2007) B1106–B1114.
[19] P.J. Ferreira, G.J. la O', Y. Shao-Horn, D. Morgan, R. Makharia, S. Kocha, H.A. Gasteiger, J. Electrochem. Soc. 152 (11) (2005) A2256–A2271.
[20] W. Bi, T.F. Fuller, J. Electrochem. Soc. 155 (2008) B215–B221.
[21] J. Xie, D.L. Wood III, K.L. More, P. Atanassov, R.L. Borup, J. Electrochem. Soc. 152 (2005) A1011–A1020.
[22] E. Guilminot, A. Corcella, F. Charlot, F. Maillard, M. Chatenet, J. Electrochem. Soc. 154 (1) (2007) B96–B105.
[23] A. Ohma, S. Suga, S. Yamamoto, K. Shinohara, J. Electrochem. Soc. 154 (8) (2007) B757–B760.
[24] D. Zhao, B.L. Yia, H.M. Zhang, M. Liu, J. Power Sources 195 (2010) 4606–4612.
[25] P. Ferreira-Aparicio, M.A. Folgado, L. Daza, J. Power Sources 192 (2009) 57–62.
[26] T.V. Nguyen, M.W. Knobbe, J. Power Sources 114 (2003) 70–79.
[27] A. Collier, H. Wang, X.Z. Yuan, J. Zhang, D.P. Wilkinson, Int. J. Hydrogen Energy 31 (2006) 1838–1854.
[28] F. Ettingshausen, J. Kleemann, M. Michel, M. Quintus, H. Fuess, C. Roth, J. Power Sources 194 (2009) 899–907.
[29] M. Hinaje, D. Nguyen, S. Raël, B. Davat, C. Bonnet, F. Lapicque, Int. J. Hydrogen Energy 34 (2009) 6364–6370.
[30] Z. Luo, D. Li, H. Tang, M. Pan, R. Ruan, Int. J. Hydrogen Energy 31 (2006) 1831–1837.
[31] T. Akita, A. Taniguchi, J. Maekawa, Z. Siroma, K. Tanaka, M. Kohyama, K. Yasuda, J. Power Sources 159 (2006) 461–467.
[32] C.G. Chung, L. Kim, Y.W. Sung, J. Lee, J.S. Chung, Int. J. Hydrogen Energy 34 (2009) 8974–8981.
[33] J. Finster, E.-D. Klinkenberg, J. Heeg, W. Braun, Vacuum 41 (1990) 1586.
[34] G. Prümper, X.J. Liu, H. Fukuzawa, K. Ueda, V. Carravetta, J. Harries, Y. Tamenori, S. Nagaoka, J. Phys.: Conf. Ser. 88 (2007) 012008, doi:10.1088/1742-6596/88/1/012008.
[35] M. Zhou, J.M. Laux, K.D. Edwards, J.C. Hemminger, B. Hong, Chem. Commun. (1997) 1977–1978.
[36] http://www.lasurface.com/database/elementxps.php.
[37] J. Tan, Y.J. Chao, M. Yang, C.T. Williams, J.W. Van Zee, J. Mater. Eng. Perform. 17 (6) (2008) 785–792.
[38] M. Schulze, T. Knöri, A. Schneider, E. Gülzow, J. Power Sources 127 (2004) 222–229.
[39] M. Schulze, M. Lorenz, T. Kaz, Surf. Interface Anal. 34 (2002) 646–651.
[40] Y. Shao, G. Yin, Y. Gao, P. Shi, J. Electrochem. Soc. 153 (6) (2006) A1093–A1097.
[41] R. Imran Jafri, T. Arockiados, N. Rajalakshmi, S. Ramaprabhu, J. Electrochem. Soc. 157 (6) (2010) B874–B879.